Journal of Wind Engineering & Industrial Aerodynamics 238 (2023) 105429

Contents lists available at ScienceDirect

Journal of Wind Engineering & Industrial Aerodynamics

journal homepage: www.elsevier.com/locate/jweia

Reducing the aerodynamic drag of high-speed trains by air blowing from the nose part: Effect of blowing speed

Zheng-Wei Chen [a,b], Guang-Zhi Zeng [a,b], Yi-Qing Ni [a,b,*], Tang-Hong Liu [c], Ji-Qiang Niu [d], Hua-Dong Yao [e]

[a] *National Rail Transit Electrification and Automation Engineering Technology Research Center (Hong Kong Branch), Hung Hom, Kowloon, Hong Kong SAR, China*
[b] *Department of Civil and Environmental Engineering, The Hong Kong Polytechnic University, Hung Hom, Kowloon, Hong Kong SAR, China*
[c] *Key Laboratory of Traffic Safety on Track, Ministry of Education, School of Traffic & Transportation Engineering, Central South University, Changsha, 410075, China*
[d] *School of Mechanical Engineering, Southwest Jiaotong University, Chengdu, 610031, Sichuan, China*
[e] *Department of Mechanics and Maritime Sciences, Chalmers University of Technology, Gothenburg, 41296, Sweden*

ARTICLE INFO

Keywords:
High-speed train
Air blowing
Blowing speed
Aerodynamic drag
Flow structure

ABSTRACT

To reduce the aerodynamic drag of high-speed trains, this work proposes an air blowing configuration on the head and tail cars of high-speed trains. The variation in the aerodynamic drag and slipstream velocity is analyzed under different blowing velocities, and the flow mechanism for train aerodynamic performance alteration is explained. The results show that under the blowing speeds of $U_b = 0.05U_t$, $0.10U_t$, $0.15U_t$, and $0.20U_t$, where U_t is the train speed, the total drag coefficient (C_d) decreases by 5.81%, 10.78%, 13.70%, and 15.43% compared to the without-blowing case, respectively. However, with the increase in the blowing speed, the reduction trend of C_d tends to be smoother; namely, the decrement ratio compared to the previous blowing speed for the head car is 9.08%, 0.11%, 0.60%, and 1.14% for $U_b = 0.05U_t$, $0.10U_t$, $0.15U_t$, and $0.20U_t$, respectively. The blowing measure generates an air gap between the coming flow and train surface, consequently causing a reduction in the viscous and pressure drag. In addition, the structure size and strength of the wake flow under different blowing cases show a decreasing trend from $U_b = 0.00U_t$ to $0.10U_t$ and then an increasing trend from $U_b = 0.10U_t$ to $0.20U_t$. Thus, considering the blowing cost, efficiency, and flow structure evolution comprehensively, the case of $U_b = 0.10U_t$ is recommended. Under this blowing speed, the reduction ratio of the aerodynamic drag is 9.18%, 12.77%, 10.90%, and 10.78% for the head, middle, tail car, and total train, respectively.

1. Introduction

High-speed trains are extremely handy, speedy, and environmentally friendly, and they are expanding globally (Kim et al., 2016; Li et al., 2017; Guo et al., 2020; Chen et al., 2022; Liu et al., 2022a). The current demands of industry and market consumption require high-speed railway systems with high operating speed, large volume, and far-distance transport capacities for commuting and freight in metropolitan circles (Guo et al., 2018a, 2018b; Huang et al., 2021). However, meeting these demands potentially brings about the problems of energy consumption and environmental protection (Huo et al., 2021a). Previous studies have indicated that the energy consumption of train running is mainly due to overcoming aerodynamic drag induced by the incoming airflow (Wang, 2012; Ding et al., 2016), but the aerodynamic drag of trains operating at high speeds increases proportionally with the square of the running speed. For a railway with running speeds higher than 300 km/h, the aerodynamic drag, for instance, makes up roughly 75–80% of the total drag (Baker, 2014; Raina et al., 2017; Zhang et al., 2018a; Xia et al., 2020; Huo et al., 2021b). As a result, reducing the aerodynamic drag of high-speed trains has become a crucial issue.

Aiming to reduce aerodynamic drag of trains, research efforts have been devoted to developing various methods to investigate the generating and control mechanism of the aerodynamic drag, including full-scale tests, wind tunnel tests, and numerical simulations (Sun et al., 2010; Chen et al., 2017, 2022; Munoz-Paniagua and García, 2020). Full-scale and wind tunnel tests of a train can provide fundamental real-world data (Gallagher et al., 2018). For instance, Lukaszewicz (2007) compared the effects of factors such as the speed, number of

---

* Corresponding author. Department of Civil and Environmental Engineering, The Hong Kong Polytechnic University, Hung Hom, Kowloon, Hong Kong SAR, China.

E-mail address: ceyqni@polyu.edu.hk (Y.-Q. Ni).

https://doi.org/10.1016/j.jweia.2023.105429
Received 18 September 2022; Received in revised form 2 April 2023; Accepted 10 April 2023

axles, etc., on the running resistance of diverse trains in full-scale experiments. Although the experimental results provide a reference for reducing running resistance and energy-efficient operation of trains, full-scale tests have typically been conducted after design of trains (Li et al., 2021a), so the measures of reducing the aerodynamic drag are usually reactive. To provide design solutions for reducing the aerodynamic drag of a high-speed train, Yang et al. (2012) conducted wind tunnel tests to compare experimental results of high-speed trains with different head shapes and analyzed the influence of head shape on the performance of reducing the aerodynamic drag. However, experiment data are limited mostly because of the difficulty of conducting experiments in real scenes and the high cost of testing different types of experimental objects (Gallagher et al., 2018; Somaschini et al., 2020).

With significant improvement in computing power, numerical simulations have been widely used in the research on reducing train aerodynamic drag because of the low cost and high capacity to conduct and refine global and local analysis (Gao et al., 2021; Li et al., 2021a). Numerical simulations have been used to optimize the head shape of trains (Chen et al., 2016; Li et al., 2016; Zhang et al., 2017b; Niu et al., 2018; Munoz-Paniagua and García, 2020) and adjust local structures (Zhang et al., 2017a, 2018a; Gao et al., 2019; Sun et al., 2020; Li et al., 2021b; Liu et al., 2022b) with intent to reduce the operating resistance of trains. However, the conventional methods for complex shape design may only lead to limited reduction in drag. For instance, Niu et al. (2018) addressed a study on extending the streamlined head of a high-speed train from 8 m to 12 m and found that the drag coefficients of the whole train decreased by 9.77%. Chen et al. (2016) achieved a decrement of 19.0% in the train's drag coefficient by extending the train's streamlined length from 5 m to 9 m, but only 4.3% decrease when the streamlined length changes from 9 m to 15 m. Therefore, recent research efforts have been made to explore new methods to reduce the aerodynamic drag of trains, one of which is the active control of turbulent flow fields. This method aims to improve the aerodynamic performance by energy excitation to change the local or even global flow field structure around an object without changing its shape (Huang et al., 2021). To evaluate the effect of different active flow control strategies on the flow field structure and drag coefficient, Minelli et al. (2016) achieved drag reduction with the use of zero net mass flux synthetic jets and identified an optimal actuation frequency in terms of induced fluctuations and drag reduction. Wang et al. (2019) analyzed the flow characteristics of near wake flow behind the 25° Ahmed models using the Large-Eddy Simulation and proposed an unsteady flow control method based on semi-sinusoidal signals, which resulted in a significant reduction of the aerodynamic drag. Other similar active flow control strategies for reducing drag force for Ahmed body and generic bluff body were also reported (Minelli et al., 2017; Zhang et al., 2018; Tebbiche and Boutoudj, 2021; Veerasamy et al., 2022; Plumejeau et al., 2023). Due to the geometric shapes and characteristic sizes of high-speed trains being different from those of airfoils, Ahmed body and generic trucks, the conclusions drawn from the above studies may be invalid to high-speed trains. In view of this, investigators have considered active control methods specific to high-speed trains, including air blowing in a particular region of train. By setting jet slots at special flow positions at the rear of the maglev train, Huang et al. (2021) investigated how the turbulent flow field was affected. Liang et al. (2022) studied the influence of different blowing speeds and blowing gas densities on the drag reduction of a high-speed train by setting jet ports on the top of the train.

As aforementioned, there is a paucity of studies that addressed the application of active control strategies to high-speed trains, and an exploration of the location of jet settings and blowing speed on the trains with the purpose of achieving the maximum potential of drag reduction helps narrow the research gap. The research on the setting of optimum parameters such as the location of jets and blowing velocity for airflow control of high-speed trains is still in its infancy. In this study, an innovative air blowing configuration on the head and tail cars is proposed to reduce the aerodynamic drag of high-speed trains. The air blowing velocity varying in relation to train running speed is analyzed to determine the most appropriate blowing speed. Also, the flow mechanisms are explored under different blowing velocities to explain changes in aerodynamic drag.

The research method and numerical model are described in Section 2 of this work. Section 3 provides results of analysis and discussions. Section 4 concludes by summarizing the main findings and suggesting themes for future research.

2. Computational model and numerical method

2.1. Train geometry

Fig. 1 shows the high-speed train model addressed in this work. It comprises three vehicles in total: a head car, a middle car, and a tail car, with lengths of 7.16h, 6.76h, and 7.16h, respectively; the width of the train is 0.92h, where h represents the train height from top of the rail and its value is 3.7 m. This study focuses on various velocities of air blowing to reduce the drag of a train, as shown in Fig. 2. The air blowing configuration is applied to the head car and tail car simultaneously. There are three air blowing positions on the streamlined area of a train, denoted by air blowing-1 (AB-1), air blowing-2 (AB-2), and air blowing-3 (AB-3). As illustrated in Fig. 2(c), AB-1 is a circular area, while AB-2 and AB-3 are not of a closed-loop shape because they have no bottom section. The space is narrowed beneath the car body, so air blowing from the bottom surface of a train may produce additional drag; namely, the air blowing may break the original smooth flow under the car body. However, there is no such problem in the upper position of a train because of the open area. Based on the blowing speeds used in previous work (Liang et al., 2022), the train speed U_t is set to 60 m/s (216 km/h), while the air blowing velocity U_b varies at four levels, i.e., $U_b = 0.05U_t$, $0.10U_t$, $0.15U_t$, and $0.20U_t$ in this study. Also, the air blowing directions of AB-1, AB-2, and AB-3 are normal to the local train surface.

2.2. Methodology and data processing

In this study, the Mach number (M_a) is calculated using the ratio of the train speed to the speed of sound, and it is less than 0.3. Following the work of Anderson Jr (2017), here the air motion is assumed to be an unsteady, viscous, incompressible flow (Liu et al., 2018). A hybrid method leveraging Reynolds-averaged Navier–Stokes equations (RANS) and Large-Eddy Simulation (LES) was used in this work. This kind of methods has been widely utilized in the research of train aerodynamics (Munoz-Paniagua et al., 2017). Specifically, to bridge the gap between the RANS and the LES, Shur et al. (2008) developed the improved delayed detached eddy simulation (IDDES) method, a hybrid RANS-LES method. Based on the grid scale, the LES and RANS zones are separated from one another. The unstable RANS model is used to mimic the pulsating motion of a small-scale vortex in the vicinity of the wall, while the LES model is used in the turbulent core position area distant from the wall area (Huo et al., 2021a, 2021b). The scale-adaptive simulation (SAS) method is a similar method, which combines the RANS and LES models and achieves accuracy compatible with IDDES but at a lower cost (Wang et al., 2017). The SAS approach introduces the von Karman length scale L_{vK} into the turbulence equations to capture the scale-adaptive temporal and spatial scales (Menter and Egorov, 2010; Rotta, 2013). The von Karman length scale L_{vK} is defined as the ratio of the first derivative to the second derivative of the velocity vector U times the von Karman constant of $\kappa = 0.41$, which can be expressed by:

$$L_{vK} = \kappa \left| \frac{U'}{U''} \right| \tag{1}$$

where,

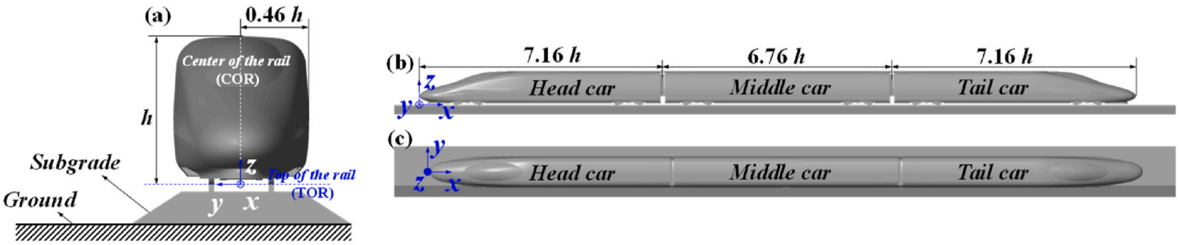

Fig. 1. The high-speed train and subgrade model: (a) front view; (b) side view; (c) top view.

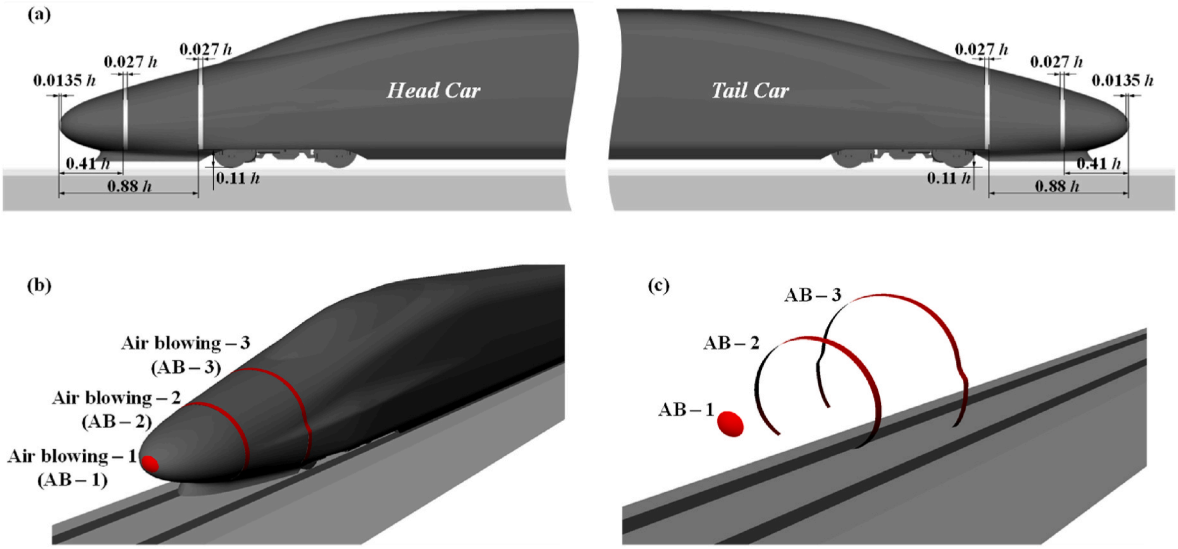

Fig. 2. Positions of air blowing on the head car and tail car.

$$U'' = \sqrt{\frac{\partial^2 U_i}{\partial x_k^2}\frac{\partial^2 U_i}{\partial x_j^2}} \tag{2}$$

$$U' = \sqrt{2 \bullet S_{ij}S_{ij}} \tag{3}$$

$$S_{ij} = \frac{1}{2}\left(\frac{\partial U_i}{\partial x_j} + \frac{\partial U_j}{\partial x_i}\right) \tag{4}$$

The inclusion of L_{vK} enables the model to adapt its length scale to resolved scales in the flow, and therefore provides sufficiently low eddy viscosity to guarantee the model functions in the LES-type mode while offering conventional RANS capabilities in the steady-flow zones. With wide applications of the hybrid RANS-LES method, the shear stress transport (SST) – SAS model has been encoded into the commercial CFD solver ANSYS Fluent (Menter, 2012). In the SST–SAS model, an additional SAS source term (Q_{SAS}), which is a function of L_{vK}, is embedded into the transport equation for the turbulence eddy frequency ω. The ω-equation dynamically and gradually switches itself from the URANS-type to the LES-type behavior when the flow is sufficiently unstable (Davidson, 2006); enormous unsteady shedding vortices around a high-speed train belong to this situation. More detailed descriptions of the SST – SAS model can be found in Menter and Egorov (2010).

In this study, the SST–SAS model is used to investigate the aerodynamic characteristics of the train. The commercial software ANSYS Fluent is used to conduct the numerical simulations with the finite volume method (FVM). The semi-implicit method for the pressure-linked equation consistent (SIMPLEC) algorithm is employed to solve the pressure–velocity coupling equation. The second-order upwind technique is used to discretize the turbulent kinetic energy and turbulent dissipation rate, while the bounded central differencing scheme is utilized to discretize the convection fluxes in the momentum equations.

The Reynolds number in this work is approximately 1.5×10^6, according to the train's speed and height. In most areas around the train, the Courant-Friedrichs-Lewy (CFL) number is roughly 1.0 since the unstable simulation has a physical time step of 5×10^{-5} s. Each time step has 30 iterations, and each turbulent equation's residual value is less than 10^{-4} to meet the convergence criteria.

In an open-air scene without ambient wind, the concerned aerodynamic parameters include the drag coefficient (C_d), lift force coefficient (C_l), and pressure coefficient (C_p), which are respectively defined as:

$$C_d = \frac{F_d}{\frac{1}{2}\rho U_t^2 A} \tag{5}$$

$$C_l = \frac{F_l}{\frac{1}{2}\rho U_t^2 A} \tag{6}$$

$$C_p = \frac{P - P_0}{\frac{1}{2}\rho U_t^2} \tag{7}$$

where F_d and F_l are the train drag and lift force, respectively; A is the reference area, which in this work represents the cross-sectional area of the train, and its value is 11.22 m^2 for a full-scale size; P is the local static pressure on the train surface; and P_0 is the reference pressure, which is 0 Pa in this work.

To facilitate analysis, the non-dimensional time t^* is defined as:

$$t^* = \frac{t \bullet U_t}{\sqrt{A}} \tag{8}$$

where t is the physical computational time.

2.3. Computational domain and mesh strategy

The computational domain is shown in Fig. 3. The entire computational domain is set as a 1/10 scale model to meet the mesh size requirement of the adopted turbulence model. The cross-sectional area is $22h \times 12h$, providing a blockage ratio in the numerical wind tunnel of 0.35%, which is less than the requirement of the EN norm of 1% (EN14067-4, 2018). The distance from the upstream boundary to the nose point of the head car is $22h$, and that from the nose point of the tail car to the downstream boundary is $44h$. Both sides are $11h$ far away from the center of the rail. The height of the computational domain is $12h$. Uniform and constant velocity profile of $U_t = 60$ m/s over time is used on the inlet. On the lateral sides and upper boundary, a symmetry wall condition is adopted. The zero-pressure outlet boundary condition ($P = 0$ Pa) is implemented at the downstream boundary; the no-slip wall boundary condition is used on the train surface. The moving no-slip wall conditions are adopted on the ground and subgrade, setting the velocity component along the flow direction equal to the free flow velocity, $\overline{u} = U_t, \overline{w} = \overline{v} = 0$. This is set to simulate the flow impact of train movement over the ground and subgrade accurately. Here the variables with an overbar represent the large-scale average components after filtering (the small-scale counterparts are obtained separately from the SGS model). For example, $\overline{u}$, $\overline{v}$, and $\overline{w}$ stand for the resolved average velocity components in the x, y, and z directions, respectively, computed from the RANS equations.

The SnappyHexmesh generator of open-source software OpenFOAM (Open Source Field Operation and Manipulation) is used to generate an unstructured hexahedral mesh. As illustrated in Fig. 4(a), three refinement boxes (i.e., coarse, fine, and extra-fine boxes) are used to ensure that detailed flow separations are captured accurately. In particular, each refinement region is symmetric along the center of the rail, and the width and height of each refinement area are $11h$ and $5.7h$ for the coarse area, $5.5h$ and $3h$ for the fine area, and $1.7h$ and $1.7h$ for the extra-fine area. Along the train length, the refinement region in the wake region of the train is set to be longer than that in the front of the train, which is used to distinguish and capture the wake flow accurately. Generally, the wake flow is turbulent and complex. As demonstrated in Fig. 4(b), the mesh in the air blowing region is finer than that of the car body so as to better describe the slight airflow motion. As is well known, the velocity gradient changes gradually near the car body due to the wall effect, so ten-layer prism meshes are attached to the concerned object to compute this change. The first layer's non-dimensional wall distance y^+ is in the range of 30–40. For all ω-equation-based models in ANSYS Fluent, the y^+-insensitive wall treatment is considered. It is realized by combining the viscous sublayer formulation with the logarithmic layer formulation based on y^+ (ANSYS, 2017). This procedure facilitates achieving dependable flow structures close to the wall.

To evaluate the effect of mesh number, we keep the refinement area unchanged but increase the mesh count in the corresponding regions. Three different mesh types, including coarse (17 million), medium (31 million), and fine (45 million) meshes, are compared. This study focuses on drag reduction, as shown in Fig. 5; the drag coefficient C_d of the head and tail cars without air blowing is used to test the mesh sensitivity. For the coarse, medium, and fine meshes, the C_d of the head car is set to 0.130, 0.137, and 0.136, respectively; the C_d of the tail car is set to 0.112, 0.127, and 0.126, respectively. Without taking into account additional disturbances, the difference in C_d between the head car under the three different mesh types is less than that of the tail car because of the direct effect of the approaching flow on the head car. In addition, the difference in the C_d value between coarse and medium meshes is larger than the difference in the C_d value between medium and fine meshes. For the head car, the difference in the drag coefficient between the coarse and medium meshes is 5.38%, while the difference between the medium and fine meshes is 0.73%. For the tail car, the difference in the drag coefficient between the coarse and medium meshes is 13.39%, while the difference between the medium and fine meshes is 0.79%. Therefore, either medium or fine mesh is acceptable, and there is no need for finer mesh. In order to accurately capture the influences caused by different blowing speeds on the aerodynamic viscous drag and pressure drag portion, the results obtained under the fine mesh are presented and analyzed in the following.

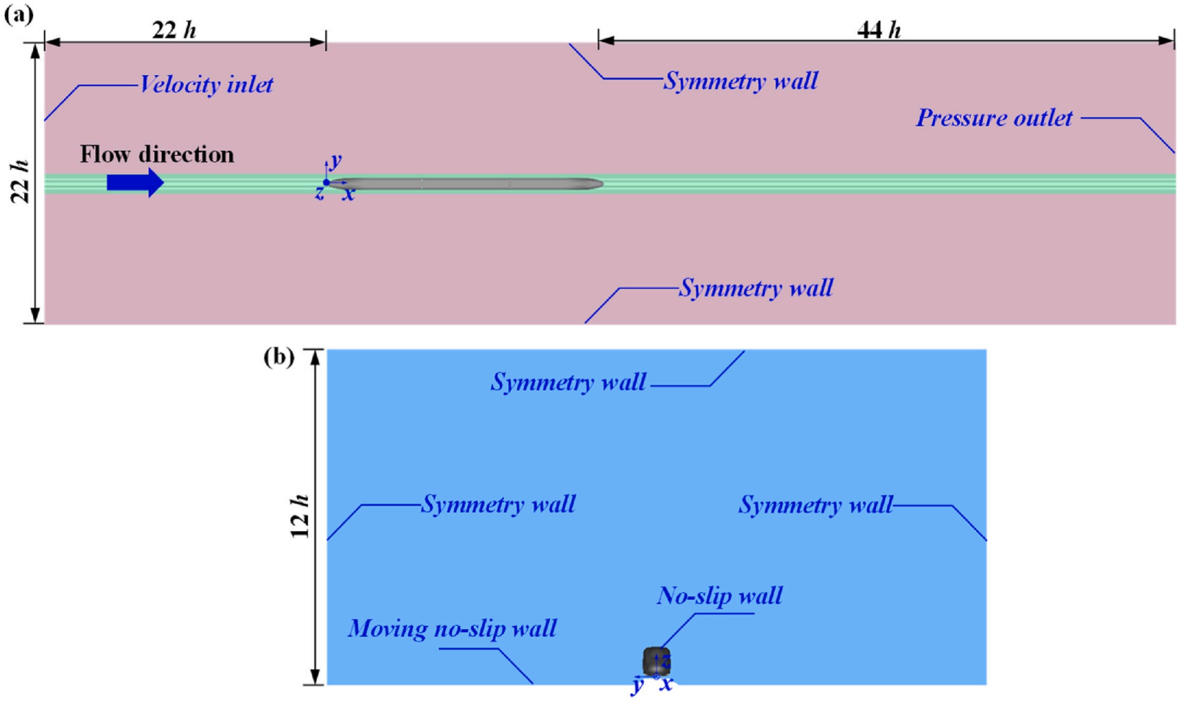

Fig. 3. Computational domain: (a) top view; (b) front view.

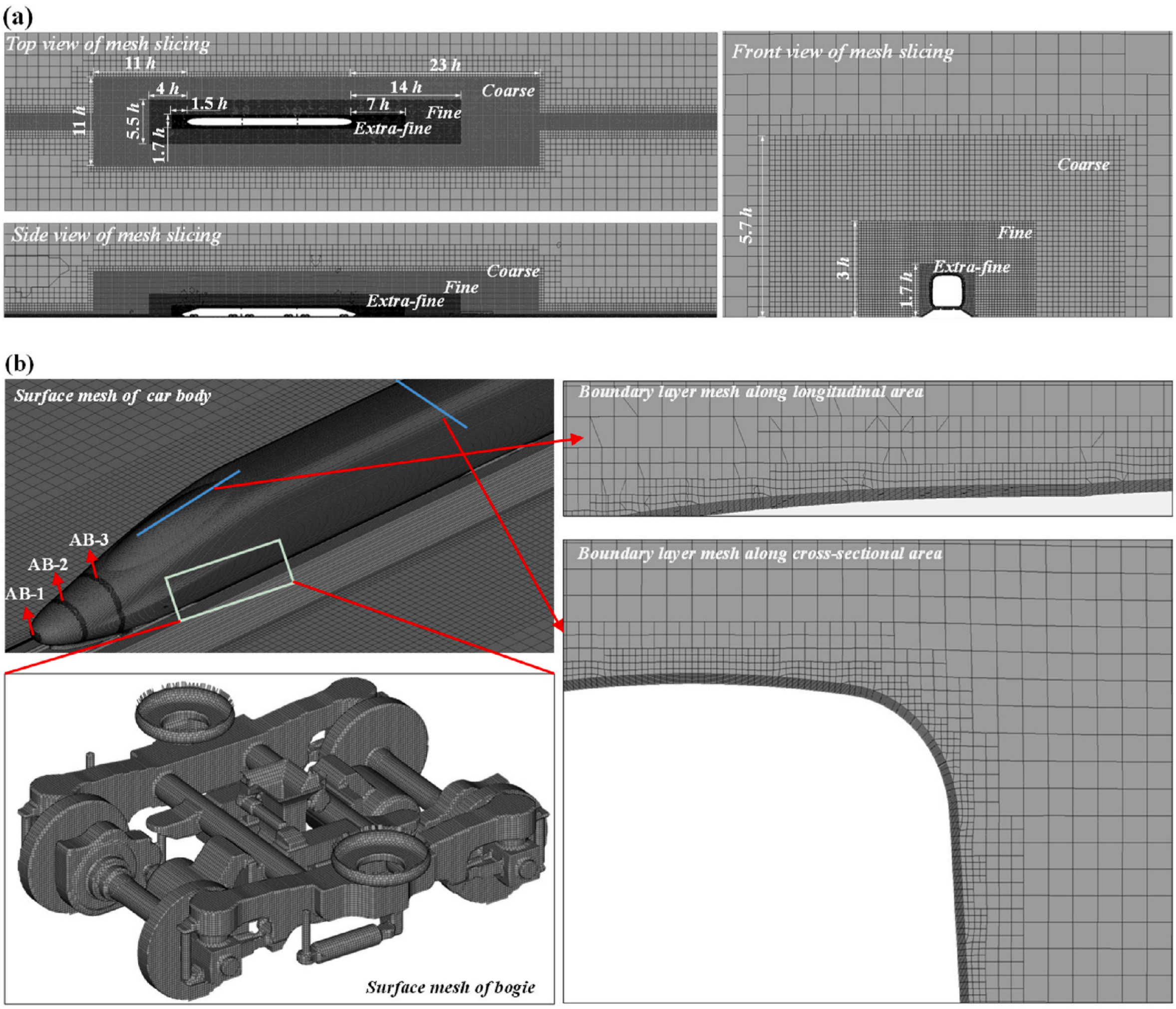

Fig. 4. The computational mesh: (a) mesh slicing; (b) surface mesh and boundary layer mesh.

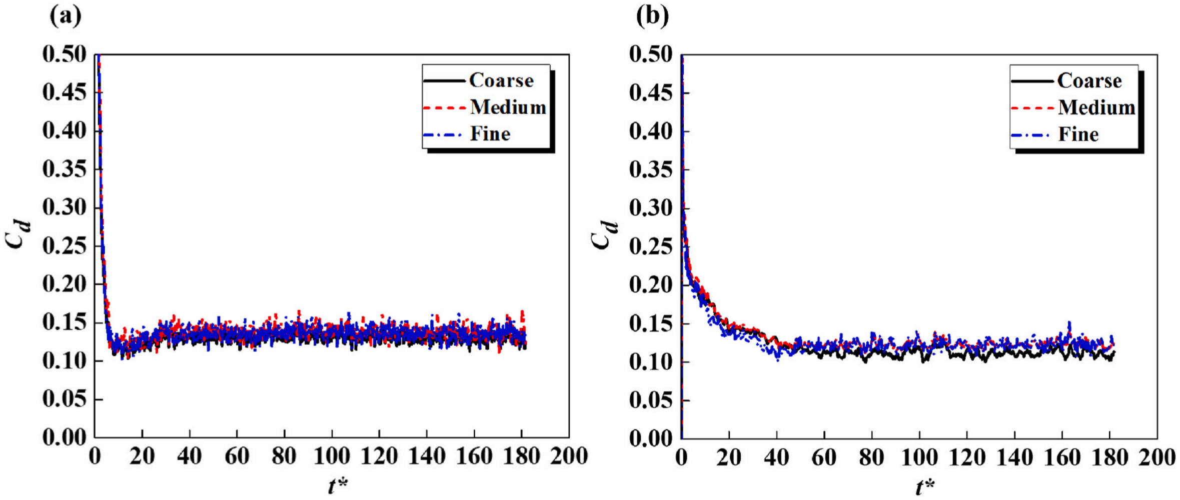

Fig. 5. Mesh sensitivity test: (a) C_d of head car; (b) C_d of tail car.

2.4. Validation of numerical results

The 1/8 sized model of a high-speed train with two cars (head car and tail car) that previously underwent wind tunnel tests (Niu et al., 2016) and the findings of the tests are used to validate this study. The test segment has a cross-sectional area of 3 m × 3 m, a length of 15 m, a test wind speed of 60 m/s, and a turbulence intensity of less than 0.5%. As for the subgrade and floor, the blocking ratio is less than 5%. Identical train model and wind tunnel dimensions are used in all numerical simulations to ensure the credibility of the verification results, while it means that the train model in the current work is not fully consistent with that in the wind tunnel experiment, e.g., the length of the train. The head and tail carriages of the railway model were employed in the wind tunnel tests. Given the inflow velocity and the train height, the Reynolds number of the wind tunnel test is calculated as 1.89×10^6. The same procedure in terms of the grid method, the numerical algorithm described in Section 2.3, and wind tunnel boundary conditions is adopted in the numerical simulations for comparison with the wind tunnel test results. Detailed information about the experiment can be found in the literature (Niu et al., 2016). Since the drag coefficient is of high interest in this study, the drag coefficients obtained in the numerical simulations and wind tunnel tests are illustrated in Fig. 6(a). The highest C_d difference between the findings of the numerical simulations and the wind tunnel tests is less than 2%, showing that there is a high degree of agreement between the two sets of data. Moreover, as shown in Fig. 6(b), the distributions of the mean pressure coefficient C_p on the streamlined zones of the head and tail cars are compared. The surface pressure distributions from the numerical simulations are consistent with those obtained in the experiment. Consequently, the validation results indicate that the numerical method, grid resolution, and other algorithms used in this study are reliable.

3. Results and discussions

3.1. Aerodynamic force characteristics

The total drag coefficient of the train under various blowing speeds is presented in Table 1. In Table 1, η donates the reduction ratio with respect to the case without air blowing, while η^* represents the decrement ratio relative to the previous blowing speed. Both indices η and η^* indicate that the decrease rate is lower under a higher blowing speed. Compared to the case without air blowing, the drag reduction is 5.81%, 10.78%, 13.70%, and 15.43% for the blowing speed from $0.05U_t$ to $0.20U_t$. However, compared to the previous blowing speed, the decrement ratio is 5.81%, 5.28%, 3.27%, and 2.00% under the blowing speed from $0.05U_t$ to $0.20U_t$. Therefore, taking into consideration the blowing cost and efficiency comprehensively, the recommended blowing speed is 0.05–$0.15U_t$.

Table 1
Total drag coefficient C_d of train and reduction and decrement rates versus blowing speed.

	$0.00U_t$	$0.05U_t$	$0.10U_t$	$0.15U_t$	$0.20U_t$
C_d	0.3682	0.3468	0.3285	0.3178	0.3114
η	–	−5.81%	−10.78%	−13.70%	−15.43%
η^*	–	–	−5.28%	−3.27%	−2.00%

The aerodynamic drag and lift coefficients are provided in Fig. 7. In Fig. 7(a), the data without a box enclosed represents the reduction ratio with respect to the case without air blowing, while the data with a box enclosed indicates the decrement ratio relative to the previous blowing speed. As shown in Fig. 7(a), compared to the case without air blowing, the reduction ratio increases with the blowing speed, and the reduction ratio values for the head car are 9.08% and 10.76% under $0.05U_t$ and $0.20U_t$, respectively. However, with the increase of blowing speed, the reduction of drag coefficient tends to be smoother. For the head car, the decrement ratio over the previous blowing speed is 9.08%, 0.11%, 0.60%, and 1.14% for the blowing speed from $0.05U_t$ to $0.20U_t$; for the same range of blowing speed, the decrement ratio is 3.28%, 7.88%, 7.06%, and 1.54%, respectively, for the tail car. However, the lift force coefficient C_l, which is provided in Fig. 7(b), is affected slightly by the blowing speed; and compared to the change in the drag force coefficient C_d, the variation in C_l could be negligible and thus is not further analyzed in this paper.

It is known that the drag consists of pressure and viscous parts, as shown in Fig. 8(a). The pressure drag of the head car decreases mostly at a lower blowing speed of $0.05U_t$. With the increase of blowing speed, there are larger interactions between the blowing airflow and coming airflow in the front of the train, so the pressure drag increases gradually, but the values of the pressure drag with blowing are all less than that without blowing. In addition, the viscous surface airflow is blown off, so the viscous drag is significantly reduced with the blowing speed. For the middle and tail cars, the viscous drag varies slightly while the pressure drag decreases continuously with the blowing speed, as shown in Fig. 8 (b) and (c).

The standard deviation (*SD*) represents the variation in the aerodynamic force magnitude around the average value and, to a certain extent, the variation in flow field intensity. In Table 2, as the blowing speed increases, the *SD* value of each car decreases gradually, indicating that the fluctuation magnitude of C_d decreases in the blowing case. However, the reduction in the *SD* value after $0.10U_t$ is slight for the head and middle cars; after $0.15U_t$ this change is nearly invisible for the tail car.

Fig. 9 portrays the Strouhal number (*St*) of C_d for each car, where the vertical axis stands for the normalized power represented by the mean squared amplitude (PMSA). The *St* value reflects the nondimensional fluctuation frequency of the flow field, which consists of the flow induced by the train and the blowing flow. As shown in the shadow portion in Fig. 9, the fluctuation frequency range of each car decreases with the blowing speed; namely, the high-frequency range is reduced gradually. This indicates that the flow field pulsation is locked at a fixed

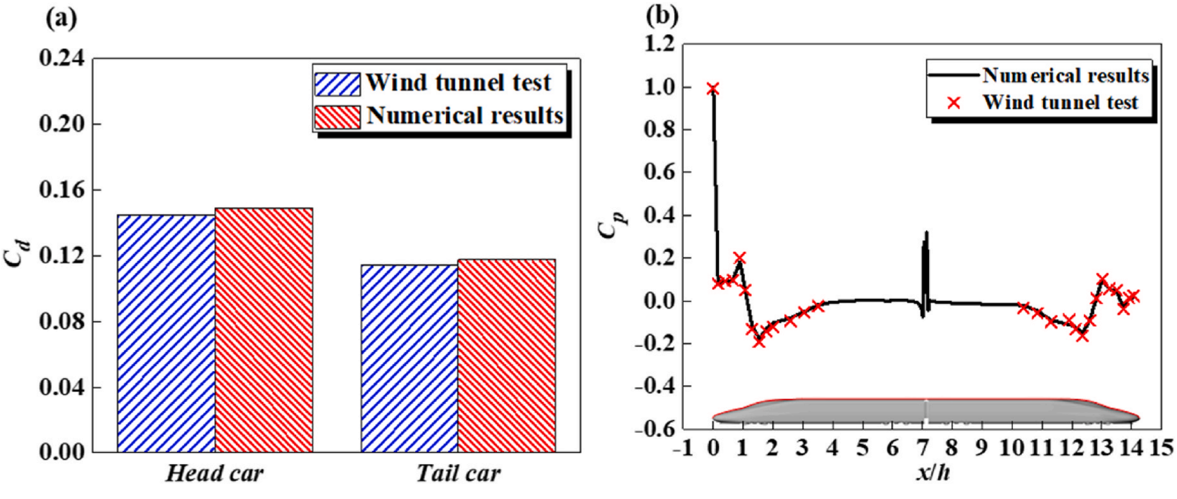

Fig. 6. Comparison between numerical and wind tunnel test results: (a) C_d; (b) C_p of the head car and tail car.

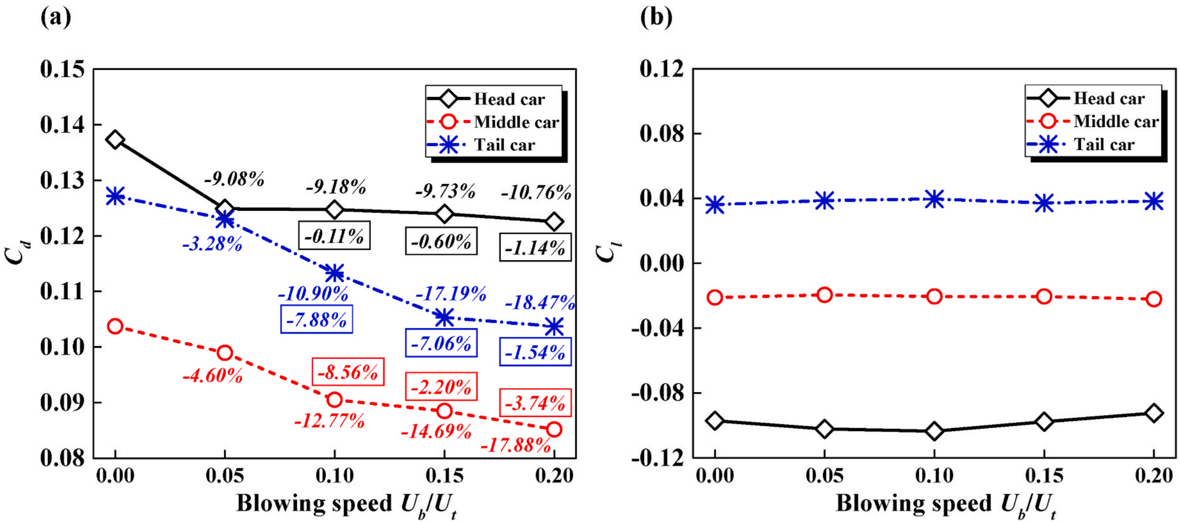

Fig. 7. Aerodynamic coefficients versus blowing speed: (a) C_d of each car; (b) C_l of each car.

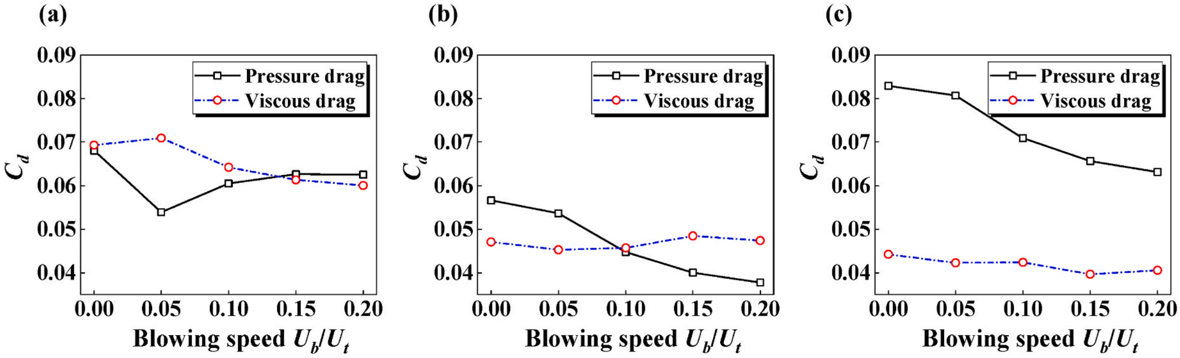

Fig. 8. Components of pressure and viscous drag: (a) head car; (b) middle car; (c) tail car.

Table 2
The standard deviation (*SD*) and mean value of aerodynamic drag coefficient C_d of each car under various blowing speeds.

	$0.00U_t$		$0.05U_t$		$0.10U_t$		$0.15U_t$		$0.20U_t$	
	SD	Mean C_d	*SD*	Mean C_d	*SD*	Mean C_dM	*SD*	Mean C_d	*SD*	Mean C_d
Head car	0.0084	0.1373	0.0076	0.1249	0.0034	0.1247	0.0037	0.1240	0.0035	0.1226
Middle car	0.0094	0.1037	0.0077	0.0989	0.0049	0.0905	0.0040	0.0885	0.0048	0.0852
Tail car	0.0077	0.1272	0.0064	0.1230	0.0061	0.1133	0.0036	0.1053	0.0033	0.1037

frequency to avoid disordered and massive flow separation. Also, the number of dominant frequencies is fewer with increasing blowing speed, especially for the head car. The first dominant frequency of the head car decreases obviously, namely, *St* is 0.66, 0.47, 0.44, 0.41, and 0.34 when the blowing speed varies from zero to $0.20U_t$, which demonstrates that the entire flow field is dominated by the larger eddy separation with a lower frequency and oscillates with smaller, regular, and higher frequency pulsation. Due to the flow disturbance of the front car, the first domain frequency of the middle and tail cars increases from zero to $0.05U_t$ and then decreases from $0.10U_t$ to $0.20U_t$.

3.2. Distributions of time-average slipstream and trackside pressure

The slipstream and pressure transient can generate various accidents, such as impacts on a worker beside a train or passengers on a platform. The blowing airflow can also disturb the original flow field around the train. Based on the EN norm (EN14067-4, 2018), this study analyzes the slipstream velocity (i.e., U_s, which is defined in Eq. (10) where U_x, U_y, and U_z are the airflow speeds in the x, y, and z directions, respectively) at a position of 3 m from the center of the rail with a height of 0.2 m above the top of the rail (Fig. 10). The variation ratio δ at this position, namely the increment or decrement of the peak value of U_s with respect to the case without air blowing, is presented in Table 3. Also, in terms of the pressure beside the track, the EN norm suggests that the range of heights to be considered should be from 1.5 m to 3.0 m above the top of the rail and at a distance of 2.5 m from the rail center. The pressure fluctuation is therefore examined in this work at a height of 2 m and a distance of 2.5 m from the rail center, as shown in Fig. 11. In Figs. 10 and 11, x/L_t represents normalized distance along the train, where L_t is the train length.

$$U_s = \frac{\sqrt{(U_x - U_t)^2 + U_y^2 + U_z^2}}{U_t} \tag{9}$$

As shown in Fig. 10(a), at a lower height of $z = 0.2$ m, there are three peak values of the slipstream velocity, corresponding to the nose of the head car (around $x/L_t = 0$), the nose of the tail car (around $x/L_t = 1$), and

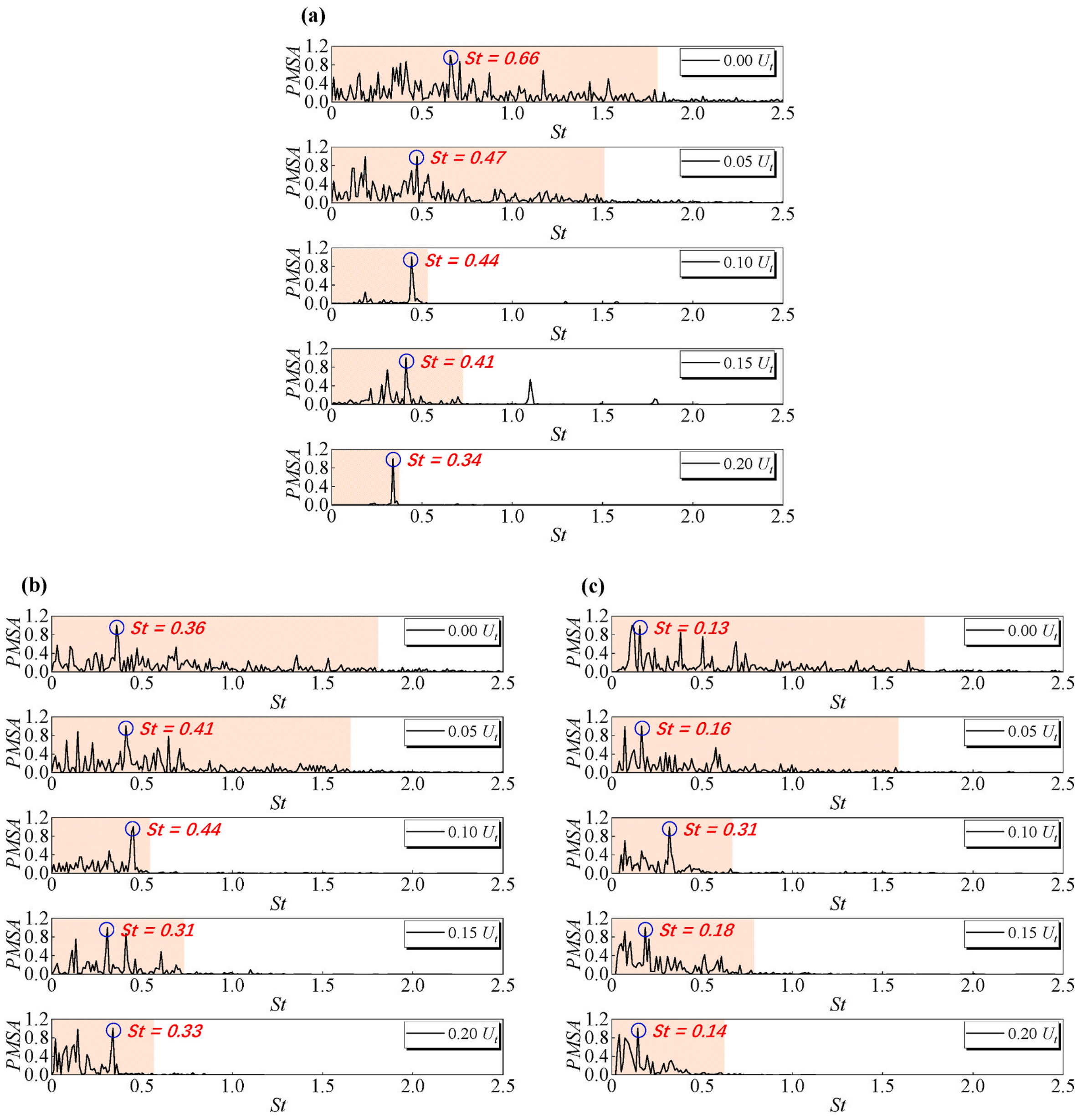

Fig. 9. The Strouhal number (St) of C_d under different blowing speeds: (a) head car; (b) middle car; (c) tail car.

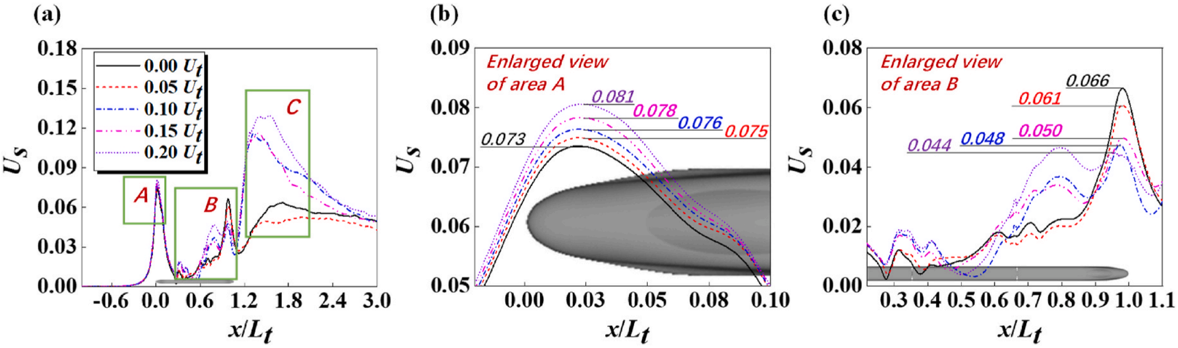

Fig. 10. Slipstream velocity U_s at a position of $y = 3$ m, $z = 0.2$ m: (a) U_s along the whole train; (b) enlarged view in the head car region; (c) enlarged view in the middle and tail car region.

Table 3
Variation ratio (δ) of peak slipstream velocity of U_s versus blowing speed at a position of $y = 3$ m, $z = 0.2$ m.

	$0.00U_t$		$0.05U_t$		$0.10U_t$		$0.15U_t$		$0.20U_t$	
	U_s	δ	U_s	δ	U_s	δ	U_s	δ	U_s	δ
Area A	0.073	–	0.075	2.74%	0.076	4.11%	0.078	6.85%	0.081	10.96%
Area B	0.044	–	0.048	−7.58%	0.050	−24.24%	0.061	−27.27%	0.066	−33.33%

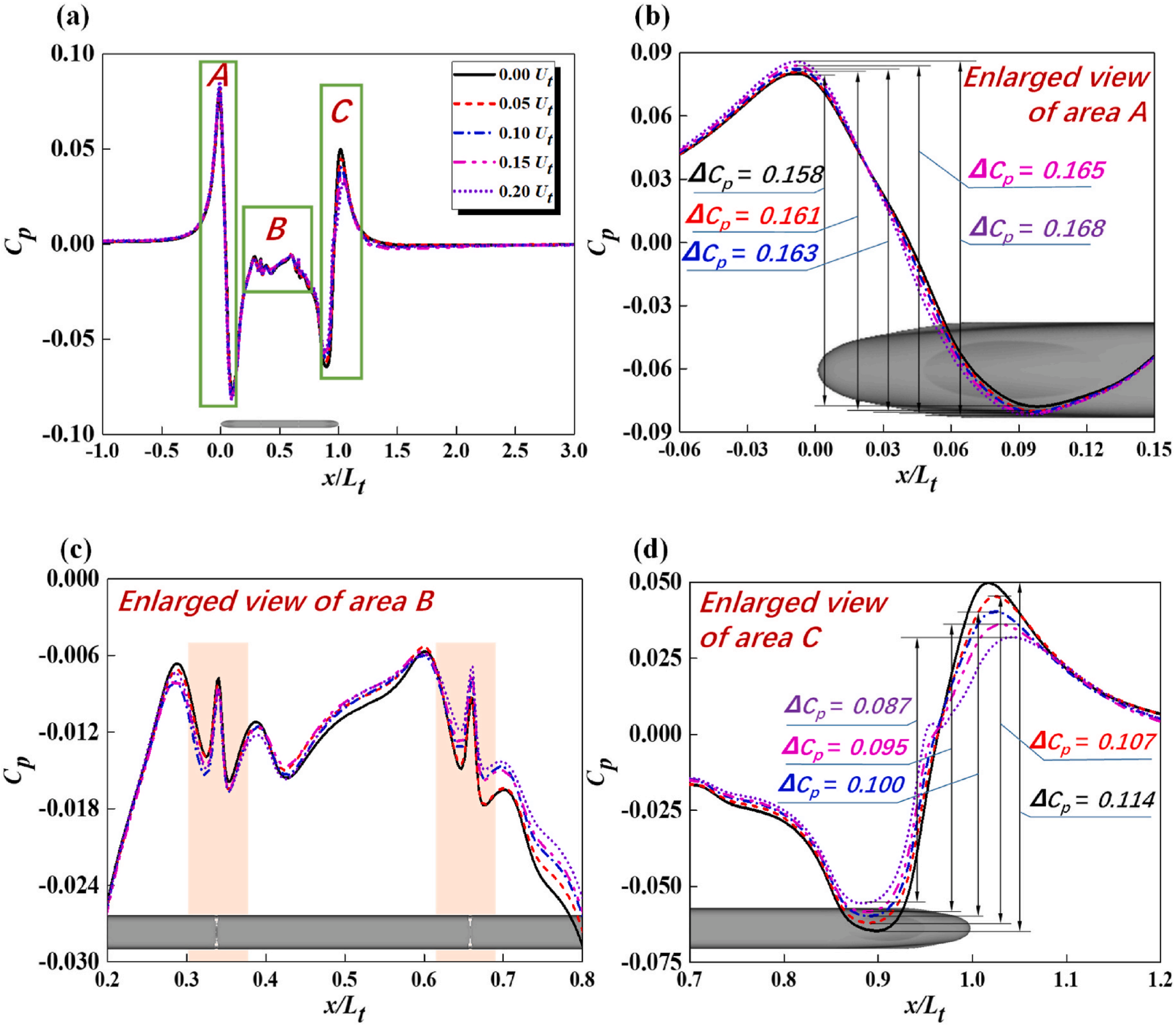

Fig. 11. Trackside pressure at a position of $y = 2.5$ m, $z = 2$ m: (a) pressure variation along the whole train; (b) enlarged view in the head car region; (c) enlarged view in the middle car region; (d) enlarged view in the tail car region.

the wake flow area after the tail car (around $x/L_t = 1.5$). In the nose portion of the head car, the airflow is compressed to a large slipstream velocity suddenly, as shown in area *A* of Fig. 10(a); and after the streamlined head part, the slipstream velocity decreases. Along the uniform cross-sectional region of the head, middle, and tail cars, the slipstream increases gradually due to the viscous effect and bogie disturbance. In the streamlined head region of the tail car, there is an airflow release effect, which causes the second peak value of the slipstream velocity in the nose point of the tail car, as shown in area *B* in Fig. 10(a). After the nose point of the tail car, the near wake flow accumulation induces the third peak value of the slipstream velocity, as shown in area *C* in Fig. 10(a).

Because of the impacting and compressive effects brought by the interaction between the ambient flow field and the local blowing airflow, as shown in Fig. 10(b), when the blowing speed rises, the peak value of U_s in region *A* likewise increases. The U_s peak value is 0.073, 0.075, 0.076, 0.078, and 0.081 under the blowing speed of zero, $0.05U_t$, $0.10U_t$, $0.15U_t$, and $0.20U_t$, respectively; the corresponding increment rate is respectively 2.74%, 4.11%, 6.85%, and 10.96% compared to the case without air blowing. As shown in Fig. 10(c), in the region of $x/L_t =$ 0.2–0.9, the fluctuation in the slipstream velocity for the blowing speeds of zero and $0.05U_t$ is relatively lower than that for the blowing speeds of $0.10U_t$, $0.15U_t$, and $0.20U_t$ due to the coupled effect of turbulence induced by complex bogie and higher blowing speed. However, in the near-wake region of $x/L_t = 1$, the second peak value of slipstream velocity occurs. Since a higher blowing speed induces the delay effect on the near-wake flow, the slipstream peak velocity decreases with the blowing speed, namely, $U_s = 0.066$, 0.061, 0.048, 0.050, and 0.044 under the blowing speed of 0–$0.20U_t$, and the corresponding decrement rate is respectively 7.58%, 24.24%, 27.27%, and 33.33% compared to the case without air blowing. As shown in Fig. 10(a), in the far-wake area *C*, only the blowing speed of $0.05U_t$ reduces the slipstream velocity; the blowing speeds of $0.10U_t$ and $0.15U_t$ correspond to the close peak values of slipstream velocity, and the blowing speed of $0.20U_t$ corresponds to the largest far-wake flow speed. These results indicate that in the far-wake region, under low blowing speeds, the flow field is smothered, but a larger blowing speed brings about extra energy into the original flow field and thus increases the slipstream velocities.

The pressure coefficient C_p beside the track at a position of $y = 2.5$ m, $z = 2$ m is shown in Fig. 11(a). There are two alternating positive-negative pressure waves in areas A and C induced by the nose of the head and tail cars, respectively. In area B, the uniform cross-sectional profile of the car body results in a relatively steady pressure except for the position of two inter-carriage gaps, as shown in Fig. 11(c). To facilitate analysis, the variation ratio ε, i.e., the increment or decrement of the peak-peak value of the pressure coefficient ΔC_p with respect to the case without air blowing, is presented in Table 4. For the head pressure wave in Fig. 11(b), the peak-peak values of the pressure coefficient ΔC_p increases with the blowing speed; the peak values of 0.158, 0.161, 0.163, 0.165, and 0.168 correspond to the blowing speed range of 0–$0.20U_t$, indicating the increment rates of 1.90%, 3.16%, 4.43%, and 6.33% compared to the case without air blowing. However, the tail pressure wave decreases when the blowing speed becomes larger, and the decrement rate is 6.14%, 12.28%, 16.67%, and 23.68% compared to the case without air blowing.

Regarding the slipstream velocity U_s and peak-peak value of pressure coefficient ΔC_p generated in the nose position of the head and tail cars, U_s and ΔC_p in the head part increase with the blowing speed, while U_s and ΔC_p in the tail part decrease with the blowing speed. The absolute values of the reduction rates of U_s and ΔC_p in the tail car position are always larger than the corresponding increase rates in the head car position under the same blowing speed.

3.3. *Drag reduction mechanism with air blowing*

For the head and tail cars, the time-average streamline of the coming flow along the center of the car is shown in Fig. 12. The results shown in Fig. 12 can be used to explain the mechanism of drag reduction illustrated in Fig. 8. It should be noted that the streamline in Fig. 12 represents the coming flow without the airflow caused by air blowing.

As shown in Fig. 12, for the head car, areas A and B represent the blowing positions of AB-1, AB-2, and AB-3, area C is the front window region of the train, and area D is the car body with a uniform cross-sectional shape. For $U_b = 0.05U_t$, due to the largest positive pressure in area A, the streamline difference between $U_b = 0.05U_t$ and $U_b = 0U_t$ is small, only a slight leading and diversion effect could be observed at the bottom of the train nose portion. However, in areas B to D, an obvious air gap occurs between the coming flow and train surface, and it is wider than that of the blowing speed being zero. Thus, the direct push effect is reduced, which explains why the pressure drag is significantly reduced in Fig. 8(a) at $U_b = 0.05U_t$. The air gap in areas B to D is in the motion region of the near-wall airflow, such airflow is dragged and fixed to run in the near-wall region by friction and viscous effects of the car surface. Therefore, as shown in Fig. 8(a), the viscous drag in the case of $0.05U_t$ is slightly larger than that of $0U_t$.

With the increase of the blowing speed from $0.10U_t$ to $0.20U_t$, an obvious leading and diversion effect makes the streamline run smoother in area A. Also, in area B, the air gap becomes wider with the blowing speed. Therefore, the pressure drag for 0.10–$0.20U_t$ is less than that of the blowing speed being zero. However, in area C, due to the stronger interaction between the coming and blowing flows, the coming flow affects the front window region directly, so the pressure drag increases when the blowing speed varies from $0.05U_t$ to $0.20U_t$, as shown in Fig. 8(a). Meanwhile, in area D, due to the higher energy of the blowing flow injected into the coming flow, the near-wall airflow is swiped clearer than that at the blowing speeds of zero and $0.05U_t$; namely, compared to the blowing cases of zero and $0.05U_t$, the air gap in area D is nearly invisible for 0.10–$0.20U_t$. Consequently, the viscous drag decreases gradually from $0.05U_t$ to $0.20U_t$, as shown in Fig. 8(a).

In regard to the tail car, areas E, F, G, and H correspond to the areas of D, C, B, and A on the head car, respectively. Although the blowing speed is different, the streamline distribution in area E is almost the same when the blowing speed varies from zero to $0.20U_t$. Due to the separation and reattachment generated by the inter-carriage gaps and thin-long car body, the former blowing effect in the head car has little influence on area E. In addition, because the dominant contribution of the viscous drag originates from area E, as aforementioned in Fig. 8(c), the viscous drag of the tail car changes barely from zero to $0.20U_t$. However, in areas G and H, the blowing airflow leads to a wider air gap with the increase of blowing speed and makes the coming flow run more smoothly. As the black arrow in Fig. 12 shows, the angle θ decreases with the blowing speed, and the trailing distance of the wake flow becomes longer. Therefore, the pressure drag reduces gradually with the blowing speed, as shown in Fig. 8(c).

The mean wall shear stress τ_w is the source of viscous drag, which is the product of dynamic viscosity of the air and normal velocity gradient. As illustrated in Fig. 13, the τ_w value of the head car is substantially greater than the tail car, particularly in the streamlined nose region. The value of τ_w alters slightly in the uniform cross-section car body area with the blowing speed. However, τ_w reduces obviously for both head and tail cars in the streamlined nose region. It should be noted due to the τ_w value of nearly zero for the tail car in the streamlined nose region, the relative drop value of viscous drag for the tail car is not obvious.

3.4. *Flow structures under different blowing cases*

After understanding the mechanism of drag variation with the blowing speed, the flow pattern and structure around the train are identified. There is a noticeable difference in the wake flow behind the tail car for $U_b = 0$–$0.20U_t$. In view of this, the wake flow is analyzed in detail, as depicted in Fig. 14. For all blowing speeds, from $x/L_t = 1.01$ to 1.30, there are two contra-rotating symmetry vortexes, and the flow field speed decreases gradually; while the size of both symmetry vortexes increases.

In more detail, at $U_b = 0$ and $x/L_t = 1.01$, there are two vortexes, denoted by $V1$ and $V2$, which are generated by the subgrade, and two vortexes, denoted by $V3$ and $V4$, which are formed by the streamlined nose of the tail car. As the distance from the tail car increases, at $x/L_t = 1.10$, vortexes $V1$ and $V3$ evolve into vortex $V3'$, and vortexes $V2$ and $V4$ evolve into vortex $V4$’. Meanwhile, some smaller vortexes are developed in region C, namely, vortexes $V5$ to $V8$, at $x/L_t = 1.20$. These trivial vortexes would dissipate at a longer distance from the tail car, as $x/L_t = 1.30$. Thus, it can be concluded that small vortexes in region C would eventually vanish. In addition, the vortex cores of $V3'$ and $V4$’ move far away from each other from $x/L_t = 1.01$ to $x/L_t = 1.30$. At $U_b = 0.05U_t$, region C shows slight fluctuations without complete vortexes.

Table 4
Variation ratio (ε) of ΔC_p versus blowing speed at a position of $y = 3$ m, $z = 1.4$ m.

	$0.00U_t$		$0.05U_t$		$0.10U_t$		$0.15U_t$		$0.20U_t$	
	ΔC_p	ε	ΔC_p	ε	ΔC_p	ε	ΔC_p	ε	ΔC_p	ε
Area A	0.158	–	0.161	1.90%	0.163	3.16%	0.165	4.43%	0.168	6.33%
Area C	0.114	–	0.107	−6.14%	0.100	−12.28%	0.095	−16.67%	0.087	−23.68%

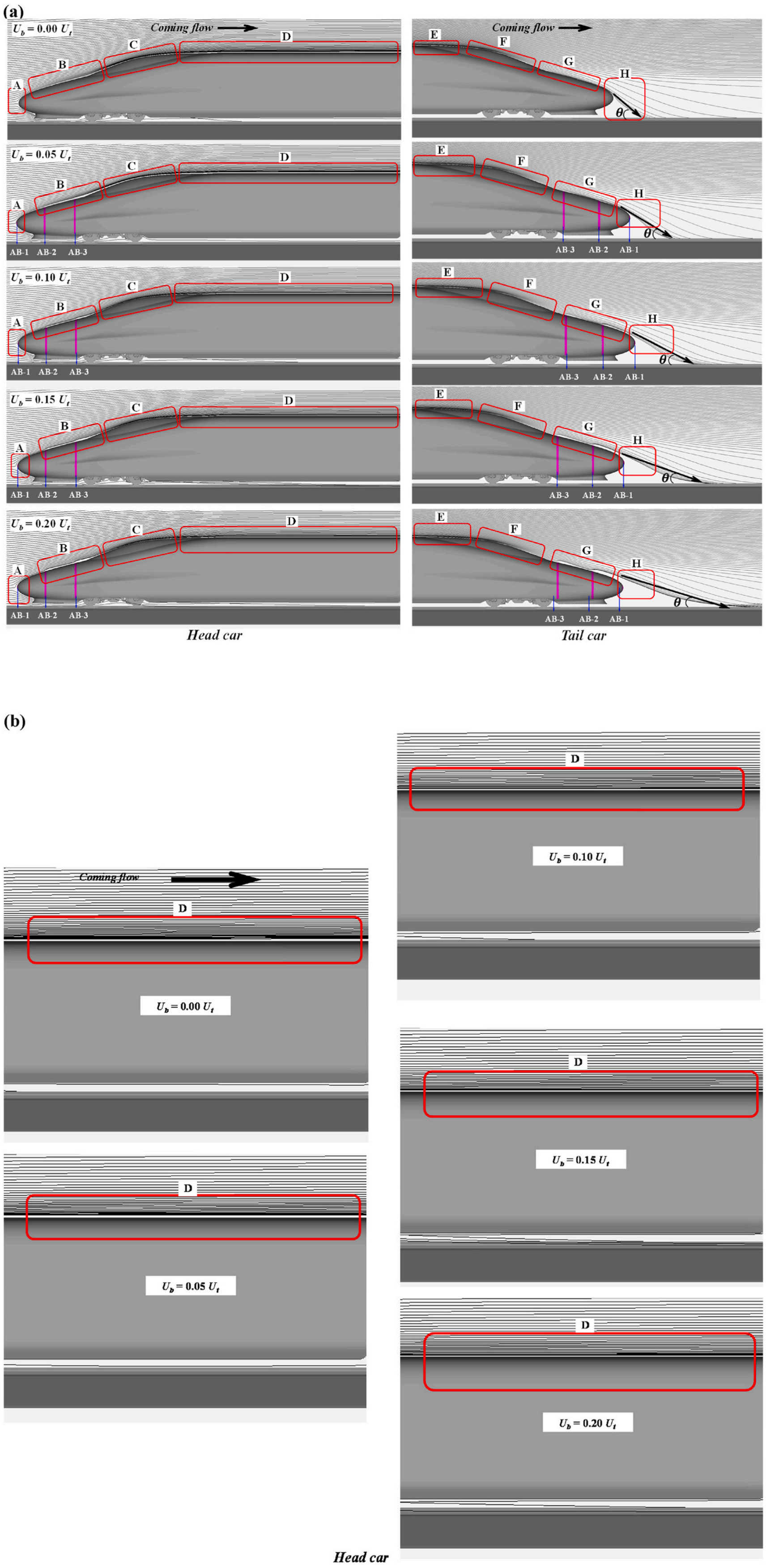

Fig. 12. (a) Time-averaged streamlines of the coming flow around the head and tail cars; (b) enlarged view of area *D*.

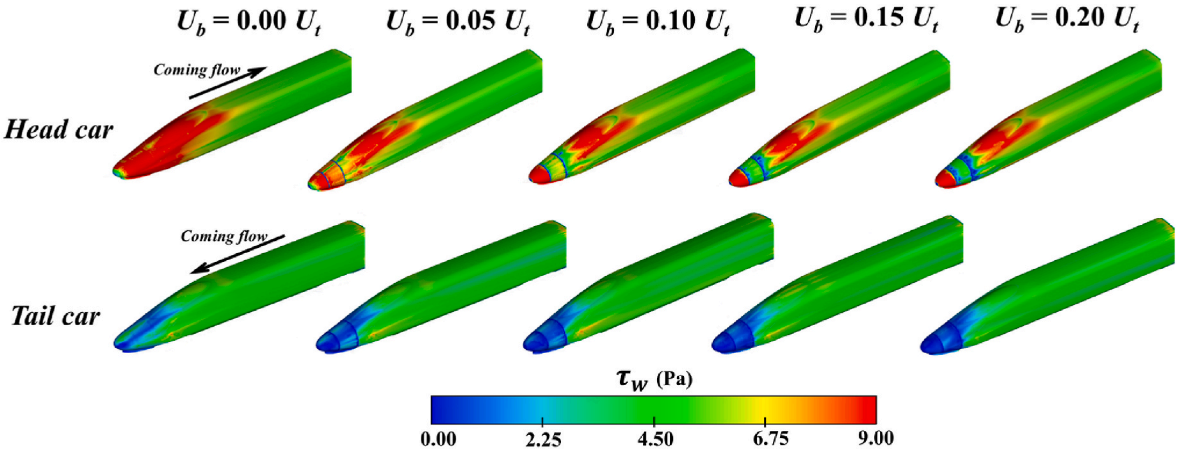

Fig. 13. τ_w on the surface of the head and tail cars.

Furthermore, with the increase of the blowing speed, at U_b = 0.10–0.20U_t, due to the strong jet flow from blowing holes, the flow in region C shows only the direct longitude motion path along the rail, there being no vortices.

Another interesting phenomenon can be observed from profiles A and B at x/L_t = 1.01 under different blowing speeds. As the blowing speed increases, profile A, where the nondimensional airflow speed U_s induced by the train is approximately 0.25, becomes lower and narrower. However, for profile B inside profile A, where the airflow speed U_s induced by the train is higher than 0.50, the profile becomes wider and higher due to the extra energy brought by the blowing airflows. These changes in the speed profile can also be observed at other positions for x/L_t = 1.10–1.30.

Fig. 15 depicts the outcomes of the vortex development around the train under various blowing speeds. The iso-surface of vortex shells, Q-criterion (unit: $1/s^2$) is used here. With the time-averaged space velocity coefficient U_s, the iso-surfaces of Q are depicted in color in Fig. 15. The value of Q is determined by:

$$Q = \frac{|\Omega|^2 - |S|^2}{2} \tag{10}$$

where Ω is the anti-symmetric and S is symmetric parts of the velocity gradient tensor, respectively.

As illustrated in Fig. 15(a), without air blowing, a mass of vortexes accumulates on both sides of the train surface in the streamlined head region. However, under the influence of air blowing, the train's surface viscosity is decreased, and the vortex buildup impact is diminished. This process is shown in the black box in Fig. 15(a). Furthermore, an enlarged view of the wake flow is provided in Fig. 15(b) to demonstrate the flow generated under different blowing speeds. At U_b = 0–0.05U_t, as the black arrow shows, there are two distinct jet flow structures in the streamlined region, and a pair of continuous counter-rotating vortexes developed along the rail. At U_b = 0.10–0.20U_t, the circular vortexes occur around the blowing slots' positions, and the counter-rotating vortexes in the wake region are invisible. In addition, the wake flow tends to move along the rail and attaches to the subgrade through a rectilinear motion. It should be noted that the vortex structure size and strength under blowing cases are all smaller than those in the no-blowing case. An interesting phenomenon is that the vortex structure size and strength exhibit a decreasing trend for U_b = 0–0.10U_t and an increasing trend for U_b = 0.10–0.20U_t. Therefore, the case of U_b = 0.10U_t is optimal among the five ones.

4. Conclusions and future work

Based on the findings of this study, the following conclusions and observations are drawn.

(1) Under the blowing speeds of 0.05U_t, 0.10U_t, 0.15U_t, and 0.20U_t, the train's overall drag coefficient drops by 5.81%, 10.78%, 13.70%, and 15.43%, respectively, compared to the no-blowing configuration. However, with the increase of the blowing speed, the reduction trend of drag coefficient decreases; the decrement ratio compared to the previous blowing speed for the head car is 9.08%, 0.11%, 0.60%, and 1.14% when the blowing speed varies from 0.05U_t to 0.20U_t;
(2) The values of U_s and ΔC_p nearby the train increase with the blowing speed in the head part of the train; while in the tail part, these values decrease gradually. The absolute values of the reduction rates of U_s and ΔC_p in the tail car position are always larger than the corresponding values of the increase rates in the head car position under the same blowing speed;
(3) The size and strength of the wake flow vortex under all blowing speeds are smaller than those of the no-blowing case; but the vortex structure size and strength show a decreasing trend for U_b = 0–0.10U_t and then an increasing trend for U_b = 0.10–0.20U_t. While all the blowing speeds considered in the current work could reduce the aerodynamic drag coefficient of a train, the optimum blowing speed is recommended to be 0.10U_t after comprehensively considering the blowing cost and efficiency.

This study investigated the efficacy of different blowing velocities in order to minimize the aerodynamic drag of high-speed trains using an active blowing technique. The focus of future research will be given on compromise between energy input needed for air blowing and energy saving generated by the train's drag reduction, synergistic effects of blowing-suction couplings, multiple blowing positions, blowing angles, etc.

CRediT authorship contribution statement

Zheng-Wei Chen: Conceptualization, Methodology, Data curation, Validation, Writing – original draft. **Guang-Zhi Zeng:** Software, Formal analysis, Investigation, Writing – original draft. **Yi-Qing Ni:** Resources, Writing – review & editing, Supervision, Funding acquisition, Project administration. **Tang-Hong Liu:** Methodology, Investigation, Validation. **Ji-Qiang Niu:** Software, Investigation. **Hua-Dong Yao:** Data curation, Visualization.

Declaration of competing interest

The authors declare that they have no known competing financial

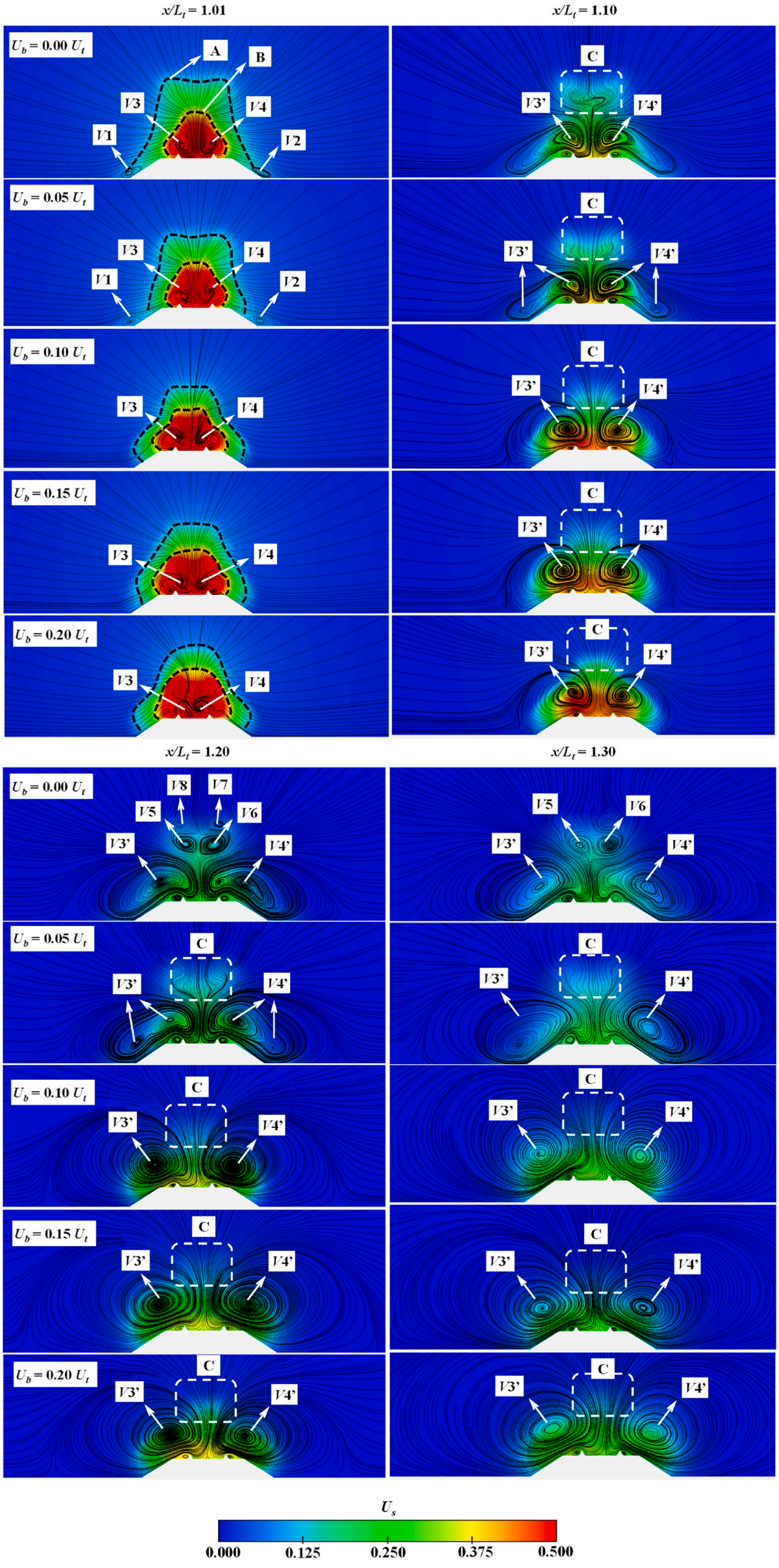

Fig. 14. Wake flow under different blowing cases.

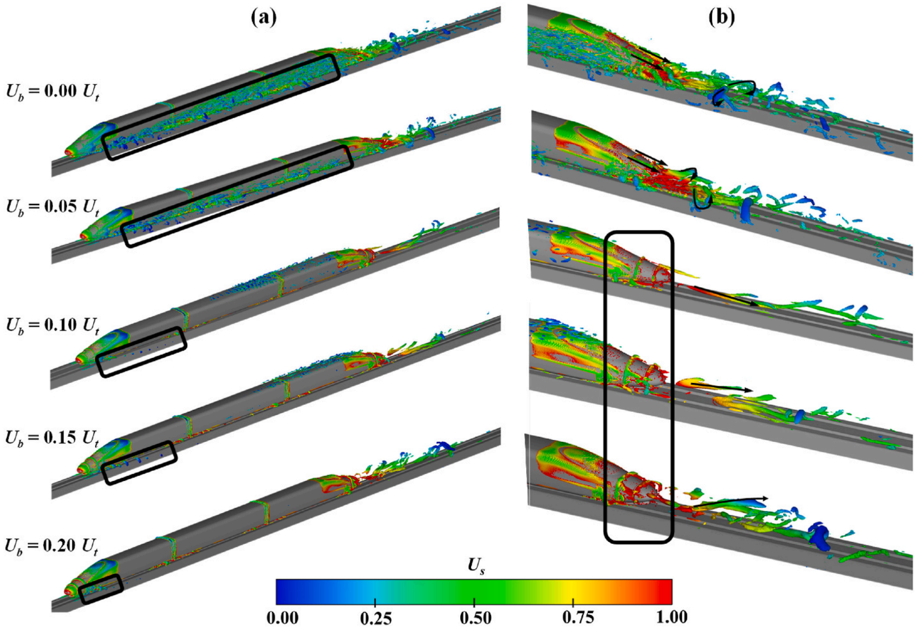

Fig. 15. Formation of a vortex around the train ($Q = 100{,}000$).

interests or personal relationships that could have appeared to influence the work reported in this paper

Data availability

Data will be made available on request.

Acknowledgements

The work described in this paper was supported by the National Natural Science Foundation of China (Grant No. 52202426, U1934209), and a grant (RIF) from the Research Grants Council of the Hong Kong Special Administrative Region (SAR), China (Grant No. R-5020-18). The authors would also like to appreciate the funding support by the Innovation and Technology Commission of the Hong Kong SAR Government (Grant No. K-BBY1), Open Project of Key Laboratory of Traffic Safety on Track of Ministry of Education, Central South University (Grant No. 502401002), The Hong Kong Polytechnic University's Postdoc Matching Fund Scheme (Grant No. 1-W16W), a grant from Wuyi University Hong Kong-Macao Joint R&D Fund (Grant No. 2021WGALH15), and Guangdong-Hong Kong-Macao Research Team Project - Guangdong Basic and Applied Basic Research Fund (Grant No. 2021B1515130006).

References

Anderson Jr., J.D., 2017. Fundamentals of Aerodynamics, sixth ed. Tata McGraw-Hill Education.
Ansys, F., 2017. ANSYS Fluent Theory Guide 18.1. ANSYS, Inc.
Baker, C., 2014. A review of train aerodynamics Part 2–Applications. Aeronaut. J. 118, 345–382.
Chen, Z., Liu, T., Chen, X., Xie, T., Li, W., 2017. Comparison of the trackside pressure with respect to different nose lengths of high-speed trains. In: Proceedings of the 2017 2nd International Conference on Industrial Aerodynamics (ICIA 2017). DEStech Transactions on Engineering and Technology Research, pp. 324–332.
Chen, Z., Liu, T., Zhou, X., Su, X., 2016. Aerodynamic analysis of trains with different streamlined lengths of heads. In: Proceedings of the 2016 IEEE International Conference on Intelligent Rail Transportation (ICIRT). IEEE, pp. 382–387.
Chen, Z., Ni, Y., Wang, Y., Wang, S., Liu, T., 2022. Mitigating crosswind effect on high-speed trains by active blowing method: a comparative study. Eng. App. Comput. Fluid Mech. 16, 1064–1081.
Davidson, L., 2006. Evaluation of the SST-SAS model: channel flow, asymmetric diffuser and axi-symmetric hill. In: Proceedings of the European Conference on Computational Fluid Dynamics. Citeseer, pp. 1–20.
Ding, S., Li, Q., Tian, A., Du, J., Liu, J., 2016. Aerodynamic design on high-speed trains. Acta Mech. Sin. 32, 215–232.
EN14067-4, 2018. Railway Applications - Aerodynamics, Part 4: Requirements and Test Procedures for Aerodynamics on Open Track. EUROPEAN COMMITTEE FOR STANDARDIZATION.
Gallagher, M., Morden, J., Baker, C., Soper, D., Quinn, A., Hemida, H., Sterling, M., 2018. Trains in crosswinds–comparison of full-scale on-train measurements, physical model tests and CFD calculations. J. Wind Eng. Ind. Aerod. 175, 428–444.
Gao, G., Li, F., He, K., Wang, J., Zhang, J., Miao, X., 2019. Investigation of bogie positions on the aerodynamic drag and near wake structure of a high-speed train. J. Wind Eng. Ind. Aerod. 185, 41–53.
Gao, H., Liu, T., Gu, H., Jiang, Z., Huo, X., Xia, Y., Chen, Z., 2021. Full-scale tests of unsteady aerodynamic loads and pressure distribution on fast trains in crosswinds. Measurement 186, 110152.
Guo, Z.-J., Liu, T.-H., Chen, Z.-W., Chen, X.-D., Jiang, Z.-H., 2018a. Different aerodynamic performances between single and double unit trains. In: Proceedings of the Third International Conference in Numerical and Experimental Aerodynamics of Road Vehicles and Trains. Events Kit Organiser.
Guo, Z., Liu, T., Chen, Z., Liu, Z., Monzer, A., Sheridan, J., 2020. Study of the flow around railway embankment of different heights with and without trains. J. Wind Eng. Ind. Aerod. 202, 104203.
Guo, Z., Liu, T., Chen, Z., Xie, T., Jiang, Z., 2018b. Comparative numerical analysis of the slipstream caused by single and double unit trains. J. Wind Eng. Ind. Aerod. 172, 395–408.
Huang, S., Yu, Y., Li, Z., Che, Z., 2021. Study of aerodynamic drag reduction of high-speed train based on tail jet-flow control. J. China Railw. Soc. 43, 38–46.
Huo, X., Liu, T., Chen, Z., Li, W., Gao, H., 2021a. Effect of the formation type with different freight vehicles on the train aerodynamic performance. Veh. Syst. Dyn. 1–29.
Huo, X., Liu, T., Chen, Z., Li, W., Gao, H., Wang, S., 2021b. Comparative analysis of the aerodynamic characteristics on double-unit trains formed by different types of high-speed train. J. Wind Eng. Ind. Aerod. 217, 104757.
Kim, Y., Lee, K., Cho, Y., Guo, Z., Koo, J., Seok, C., 2016. Fatigue safety evaluation of newly developed contact wire for eco-friendly high speed electric railway system considering wear. Int. J. Precis. Eng. Manuf. Green Technol. 3, 353–358.
Li, R., Xu, P., Peng, Y., Ji, P., 2016. Multi-objective optimization of a high-speed train head based on the FFD method. J. Wind Eng. Ind. Aerod. 152, 41–49.
Li, T., Dai, Z., Liu, J., Wu, N., Zhang, W., 2021a. Review on aerodynamic drag reduction optimization of high-speed trains in China. J. Traffic Transport. Eng. 21, 59–80.
Li, T., Dai, Z., Yu, M., Zhang, W., 2021b. Numerical investigation on the aerodynamic resistances of double-unit trains with different gap lengths. Eng. App. Comput. Fluid Mech. 15, 549–560.
Li, Z., Yang, M., Huang, S., Liang, X., 2017. A new method to measure the aerodynamic drag of high-speed trains passing through tunnels. J. Wind Eng. Ind. Aerod. 171, 110–120.
Liang, X., Luo, Z., Li, X., Xiong, X., Zhang, X., 2022. Drag reduction of high-speed trains via low-density gas injection. AIP Adv. 12, 065115.
Liu, T., Chen, Z., Zhou, X., Zhang, J., 2018. A CFD analysis of the aerodynamics of a high-speed train passing through a windbreak transition under crosswind. Eng. App. Comput. Fluid Mech. 12, 137–151.
Liu, T., Wang, L., Chen, Z., Gao, H., Li, W., Guo, Z., Xia, Y., Huo, X., Wang, Y., 2022a. Study on the pressure pipe length in train aerodynamic tests and its applications in crosswinds. J. Wind Eng. Ind. Aerod. 220, 104880.
Liu, W., Ji, Z., Guo, D., Yang, G., Zhou, G., Ren, K., 2022b. Effects of bottom deflectors on aerodynamic drag reduction of a high-speed train. Acta Mech. Sin. 38, 1–15.

Lukaszewicz, P., 2007. Running resistance-results and analysis of full-scale tests with passenger and freight trains in Sweden. Proc. Inst. Mech. Eng. - Part F J. Rail Rapid Transit 221, 183–193.

Menter, F., Egorov, Y., 2010. The scale-adaptive simulation method for unsteady turbulent flow predictions. Part 1: theory and model description. Flow, Turbul. Combust. 85, 113–138.

Menter, F.R., 2012. Best practice: scale-resolving simulations in ANSYS CFD. ANSYS Germany GmbH 1, 1–70.

Minelli, G., Hartono, E.A., Chernoray, V., Hjelm, L., Krajnović, S., 2017. Aerodynamic flow control for a generic truck cabin using synthetic jets. J. Wind Eng. Ind. Aerod. 168, 81–90.

Munoz-Paniagua, J., Garcia, J., 2020. Aerodynamic drag optimization of a high-speed train. J. Wind Eng. Ind. Aerod. 204, 104215.

Munoz-Paniagua, J., Garcia, J., Lehugeur, B., 2017. Evaluation of RANS, SAS and IDDES models for the simulation of the flow around a high-speed train subjected to crosswind. J. Wind Eng. Ind. Aerod. 171, 50–66.

Minelli, G., Krajnovic, S., Basara, B., Noack, B.R., 2016. Numerical investigation of active flow control around a generic truck A-pillar. Flow, Turbul. Combust. 97, 1235–1254.

Niu, J., Liang, X., Zhou, D., 2016. Experimental study on the effect of Reynolds number on aerodynamic performance of high-speed train with and without yaw angle. J. Wind Eng. Ind. Aerod. 157, 36–46.

Niu, J., Wang, Y., Zhang, L., Yuan, Y., 2018. Numerical analysis of aerodynamic characteristics of high-speed train with different train nose lengths. Int. J. Heat Mass Tran. 127, 188–199.

Plumejeau, B., Keirsbulck, L., Basley, J., Lippert, M., Delprat, S., Abassi, W., 2023. Drag mitigation by steady blowing and Coanda effect on a square back Ahmed body. Eur. J. Mech. B Fluid 98, 80–91.

Raina, A., Harmain, G., Haq, M.I.U., 2017. Numerical investigation of flow around a 3D bluff body using deflector plate. Int. J. Mech. Sci. 131, 701–711.

Rotta, J.C., 2013. Turbulente Strömungen: eine Einführung in die Theorie und ihre Anwendung. Springer-Verlag.

Shur, M.L., Spalart, P.R., Strelets, M.K., Travin, A.K., 2008. A hybrid RANS-LES approach with delayed-DES and wall-modelled LES capabilities. Int. J. Heat Fluid Flow 29, 1638–1649.

Somaschini, C., Argentini, T., Brambilla, E., Rocchi, D., Schito, P., Tomasini, G., 2020. Full-scale experimental investigation of the interaction between trains and tunnels. Appl. Sci. 10, 7189.

Sun, Z., Song, J., An, Y., 2010. Optimization of the head shape of the CRH3 high speed train. Sci. China Technol. Sci. 53, 3356–3364.

Sun, Z., Wang, T., Wu, F., 2020. Numerical investigation of influence of pantograph parameters and train length on aerodynamic drag of high-speed train. J. Cent. S. Univ. 27, 1334–1350.

Tebbiche, H., Boutoudj, M.S., 2021. Active flow control by micro-blowing and effects on aerodynamic performances. Ahmed body and NACA 0015 airfoil. Int. J. Fluid Mech. Res. 48 (2), 29–46.

Veerasamy, D., Tajik, A.R., Pastur, L., Parezanović, V., 2022. Effect of base blowing by a large-scale fluidic oscillator on the bistable wake behind a flat-back Ahmed body. Phys. Fluids 34 (3), 035115.

Wang, B.X., Yang, Z.G., Zhu, H., 2019. Active flow control on the 25° Ahmed body using a new unsteady jet. Int. J. Heat Fluid Flow 79, 108459.

Wang, S., Bell, J.R., Burton, D., Herbst, A.H., Sheridan, J., Thompson, M.C., 2017. The performance of different turbulence models (URANS, SAS and DES) for predicting high-speed train slipstream. J. Wind Eng. Ind. Aerod. 165, 46–57.

Wang, T., 2012. Research on measure method of high-speed train operation consumption. Railw. Transp. Econ. 34, 88–92.

Xia, Y., Liu, T., Gu, H., Guo, Z., Chen, Z., Li, W., Li, L., 2020. Aerodynamic effects of the gap spacing between adjacent vehicles on wind tunnel train models. Eng. App. Comput. Fluid Mech. 14, 835–852.

Yang, G., Guo, D., Yao, S., Liu, C., 2012. Aerodynamic design for China new high-speed trains. Sci. China Technol. Sci. 55, 1923–1928.

Zhang, B.F., Liu, K., Zhou, Y., To, S., Tu, J.Y., 2018. Active drag reduction of a high-drag Ahmed body based on steady blowing. J. Fluid Mech. 856, 351–396.

Zhang, J., Wang, J., Wang, Q., Xiong, X., Gao, G., 2018a. A study of the influence of bogie cut outs' angles on the aerodynamic performance of a high-speed train. J. Wind Eng. Ind. Aerod. 175, 153–168.

Zhang, L., Zhang, J., Li, T., Zhang, W., 2017a. Influence of pantograph fixing position on aerodynamic characteristics of high-speed trains. J. Mod. Transport. 25, 34–39.

Zhang, L., Zhang, J., Li, T., Zhang, Y., 2017b. Multi-objective aerodynamic optimization design of high-speed train head shape. J. Zhejiang Univ. - Sci. 18, 841–854.